

Article

TOF Analysis of Ions Accelerated at High Repetition Rate from Laser-Induced Plasma

Evan Russell ^{1,*}, Valeria Istokskaia ^{2,3} , Lorenzo Giuffrida ² , Yoann Levy ⁴, Jaroslav Huynh ⁴ ,
Martin Cimrman ^{3,4}, Martin Srmž ⁴ and Daniele Margarone ^{1,2} 

¹ Centre for Plasma Physics, School of Mathematics and Physics, Queen's University of Belfast, Belfast BT7 1NN, UK

² ELI-Beamlines Center, Institute of Physics, Czech Academy of Sciences, Za Radnicí 835, 252-41 Dolní Břežany, Czech Republic

³ Faculty of Nuclear Sciences and Physical Engineering, Czech Technical University in Prague, Břehová 7, 115-19 Prague, Czech Republic

⁴ HiLASE Centre, FZU-Institute of Physics of the Czech Academy of Sciences, Za Radnicí 828, 252-41 Dolní Břežany, Czech Republic

* Correspondence: erussell12@qub.ac.uk

Abstract: The generation, detection, and quantification of high-energy proton spectra that are produced from laser-target interaction methodologies is a field of increasingly growing popularity over the last 20 years. Generation methods such as target normal sheath acceleration or similar allow for collimated laminar ion beams to be produced in a compact environment through the use of short-burst terawatt lasers and are a growing field of investment. This project details the development and refinement of a python-based code to analyze time-of-flight ion spectroscopy data, with the intent to pinpoint the maximum proton energy within the incident beam to as reliable and accurate a value as possible within a feasible processing time. TOF data for 2.2×10^{16} W/cm² intensity laser shots incident on a 2 mm Cu target that were gathered from the PERLA 1 kHz laser at the HiLASE center were used as training and testing data with the implementation of basic machine learning techniques to train these methods to the data being used. These datasets were used to ensure more widely applicable functionality, and accurate calculation to within 1% accuracy of an assumed correct value was seen to be consistently achievable for these datasets. This wider functionality indicates a high level of accuracy for previously unseen TOF datasets, regardless of signal/noise levels or dataset size, allowing for free use of the code in the wider field.

Keywords: time of flight ion spectroscopy; laser induced plasma; data processing



Citation: Russell, E.; Istokskaia, V.; Giuffrida, L.; Levy, Y.; Huynh, J.; Cimrman, M.; Srmž, M.; Margarone, D. TOF Analysis of Ions Accelerated at High Repetition Rate from Laser-Induced Plasma. *Appl. Sci.* **2022**, *12*, 13021. <https://doi.org/10.3390/app122413021>

Academic Editor: Dawei Liu

Received: 24 October 2022

Accepted: 8 December 2022

Published: 19 December 2022

Publisher's Note: MDPI stays neutral with regard to jurisdictional claims in published maps and institutional affiliations.



Copyright: © 2022 by the authors. Licensee MDPI, Basel, Switzerland. This article is an open access article distributed under the terms and conditions of the Creative Commons Attribution (CC BY) license (<https://creativecommons.org/licenses/by/4.0/>).

1. Introduction

Due to a range of applications spanning medical treatment [1,2] to nuclear research [3–7], the generation of high-energy proton spectra is a field of increasing necessity over recent decades. Non-conventional methods of acceleration are heavily sought after in the hopes of more regularly achievable, compact, and affordable methods of key energy beam generation. For laser intensities within the range of 10^{18} – 10^{20} W/cm² incident on a target surface, target normal sheath acceleration (TNSA) [8] is the dominant mechanism for electron generation. Interacting with the laser, the target undergoes thermal heating and effectively instantaneous plasma ablation [9,10]. The resulting sea of free electrons travel through the target body to the rear surface with some passing through the target's rear boundary. This results in a net imbalance of charge within the target, causing a boundary field acting to restrict the electrons to grow with each successfully expelled electron. Ultimately this process halts when the sheath field becomes large enough to restrict escape entirely, reaching electric field strengths on the order of teravolt/meter. This field is strong enough to induce ionization to latent hydrocarbon contaminants, accelerating them over a short distance to extremely high velocities. Due to the

non-linearity of the electron density as they travel across the target, the electric field magnitude varies per point, thus creating a distribution of ion kinetic energies.

Often for lesser laser intensities (10^{16} W/cm²), similar results can be produced to those from the TNSA mechanism which is thus dubbed a “TNSA-like” mechanism. The functionality of this mechanism is covered in more relevant detail in Section 2. Figure 1 shows an example the energy distribution of accelerated surface contaminant hydrocarbons (primarily hydrogen ions) that were obtained from TNSA-like ion acceleration incident on a 2 mm thickness copper target, with a laser intensity 2.2×10^{16} W/cm² detected via Faraday cups. As can be seen, the number of ions decreases exponentially with increasing energy values, tending towards the signal noise threshold.

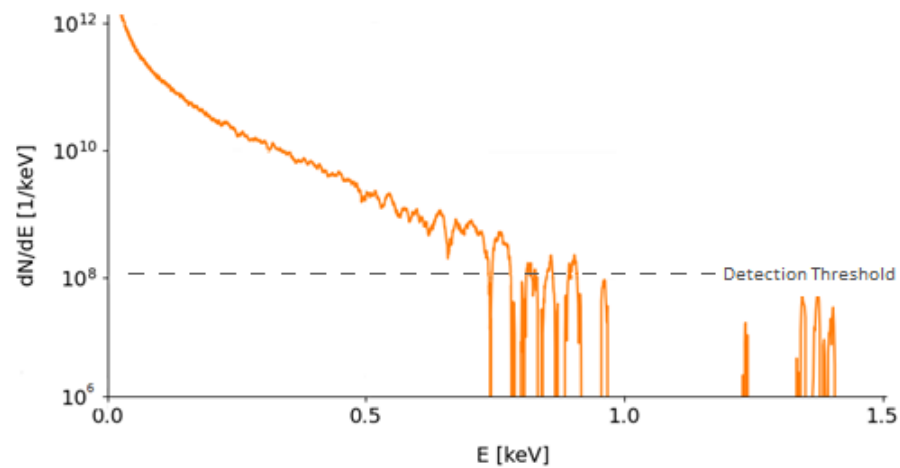


Figure 1. Typical energy distribution obtained from residual ion acceleration. Data gathered from an experimental campaign that was performed at HiLASE centre, intensity 2.2×10^{16} W/cm² laser shots incident on a 2 mm Cu target. Detection threshold marks (in KeV) the value at which the signal noise becomes equal to the signal received, disallowing accurate detection below it.

Analysis of TNSA and TNSA-like spectral data is a field of booming popularity over the past few years, and subsequently the need for adequate and timely processing of such vast quantities of data is the limiting factor of our advancement. Until recently, for low repetition rate systems, identification of the maximum proton energy within the spectrum could feasibly be done by eye, however newer studies require an automatic process without sacrificing reliability. This requirement of online processing stems from the availability of new cutting-edge laser systems operating at PW-class peak power and 1–10 Hz repetition rate, as well as sub-TW class peak power at 1 kHz [11]. This allows for the gathering of a substantial number of datasets, necessitating the need for an online identification system over the time-consuming method of manual identification.

This paper details the functionality and creation of a program that was designed to detect the maximum proton energy of laser-accelerated ion beams to as high an accuracy as feasibly achievable from the noise background. Development of the code maintained a focus on obtaining an adequate processing time without a compromise of accuracy. The code is freely available upon request to the author. The obtaining of the experimental data is also detailed below.

2. Experimental Setup

An experiment was conducted at the HiLASE center, Czech Republic, overseen by the Institute of Physics [12], to gather a series of laser-interaction datasets. Data were obtained from PERLA 1 kHz laser at intensities of 2.2×10^{16} W/cm² with a 2 mm Cu target.

In total, 24 laser shots were gathered under fixed conditions. Figure 2 shows a basic schematic of the experimental setup. The laser was fired for a ~ 1.5 ps burst with 1030 nm central wavelength and maximum laser energy up to 20 mJ at a 2 mm Cu target, with a

Faraday cup detector working in the time-of-flight technique positioned normal to the target in a backwards direction at a distance 0.18 m from the target, with a laser intensity with a magnitude of 10^{16} W/cm² and varying laser focal radius. This slight changing in laser focus results from the fact that laser-target collision induces a slight ‘boring’ effect causing the target to bend inwards, indenting and warping the surface. This additionally induces a slight, albeit largely negligible change to the intensity. The experiment was conducted within a vacuum chamber, and the detector was negatively biased (100 V) to repel incident plasma electrons that were travelling with the ion beam.

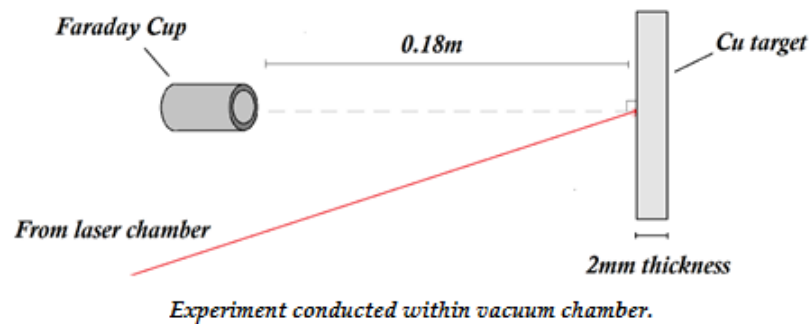


Figure 2. Schematic of laser-target collision chamber with 1030 nm central wavelength laser, 1.5 ps shot duration incident on a 2 mm Cu thickness target. The Faraday cup collector is positioned normal to back scatter. Capacitor/resistor/amplifier setup contained within the Faraday cup.

As the incident laser intensity was sufficiently low, the ion acceleration mechanism that occurred in the target backward direction is within the TNSA-like regime. Due to the low laser contrast during the experiment (10^{-3}), a significant overdense preplasma plume was generated prior to the arrival of the main pulse. Thus, on the contrary to the classical TNSA, the main acceleration direction of the ions was opposite to the gradient of density of the preplasma plume rather than of the initial target, i.e., not necessarily is in the target normal direction as suggested in particle-in-cell simulations that are described in [13].

The primary component of interest in the above setup is that of the Faraday cup ion collector. While a range of ion collectors following similar methods exist, the most readily improved and prominent of these remains to be the Faraday cup due to its reliability and simplicity. A Faraday cup at its most basic level consists of a conductive open-sided cylinder connected as a node in series to a signal amplifier. Charged particles impinging on the metallic surface are absorbed or otherwise transfer that charge to the metal which evenly distributes across the cups outer surface, building a potential difference. The plate is regularly and routinely discharged allowing a current to flow across it, which is amplified by a capacitor/resistor/amplifier parallel setup (for more detail on the Faraday cup mechanics and functionality see [14]). The voltage V_{out} that is measured in a given time is, therefore, proportional to the total number of charged particles striking the target in that time [14,15]. The collector is additionally often biased at a negative potential to repel electrons within the incident plasma stream to prevent inaccurate reduction of the perceived charge via negative charge transfer [16]. The nature of the signal generation makes accuracy of the incident particles energy more complex, however, as both a high energy and low energy proton will induce the same inherent signal in the detector. From time-of-flight (TOF) measurements [17] in which the arrival signal is measured as a function of time, the particle energy can instead be calculated using the arrival time (which will be covered in greater detail later), hence there is a requirement for online, real-time diagnostics setups circumventing the Faraday cups most significant drawback.

This, however, necessitates the inclusion of a discharge rate for the Faraday cup that is sufficiently high to ensure usable resolution of the data. Faraday cups often achieve a relative lower time resolution (typically on the nanosecond regime) due to the discharging rates fixed value being far lower than that which is achievable by other available detectors

(such as the sub-picosecond response time of the diamond detector), however they can be situationally preferred due to their high resistance to electromagnetic components.

However, photopeak detection from Faraday cups follow a more unique generation process than the previously mentioned ion load. Incident XUV rays are absorbed by valence delocalized electrons within the metallic cups surface, causing expulsion of the electron and, therefore, a net positive charge buildup leading to a detectable photopeak signal. Due to the unique, high-energy method of signal production, Faraday cups often produce photopeaks of much lower amplitude in comparison to rival signal detection systems such as diamond detectors. Indeed, the photopeak magnitude is often a fraction of that reached by the ion load.

The emission of secondary electrons remains a principal complication of Faraday cup function. As the ions kinetic energy often greatly exceeds that of the materials work function, free electrons can be emitted, causing a larger imbalance of charge. Furthermore, multiple electrons can be emitted per ion causing a potentially extravagant margin of error. Techniques have been developed to combat this process, such as optimal Faraday cup shapes or graphite shielding [16] which allow Faraday cups to maintain a reliable accuracy for TOF calculation. The energy distribution can also be derived from these data via the following equation [14]:

$$\frac{dN_i}{dE_i} = \frac{Lm_i^{\frac{1}{2}} i(t)}{e(8E_i)^{\frac{3}{2}}} \quad (1)$$

where N_i represents the number of ions in an energy interval dE_i , $i(t)$ is the current produced for a time-of-flight t , L is the detection distance, e is the electronic charge, m_i is the ion mass, and E_i is the ion energy.

The datasets that were gathered via the Faraday cup as described above were used as testing data during code development, and the varying intensity allowed the functionality of the code to be scrutinized for a range of S/N ratios. Figure 3 shows the TOF plot for two of the provided datasets, with the largest and smallest amplitude of the datasets provided respectively. The x -axis has been adjusted to allow the photopeaks to lie on the zero-line for each shot, however due to the Faraday cups reduced photopeak signal strength, as well as the back side oriented detection setup (TNSA detection favors forward orientation), the photopeak is significantly smaller than in typical TNSA-like TOF datasets. This is arguably ideal for the development of identification software, as the codes' ability to detect the minimum possible photopeak signal can be scrutinized.

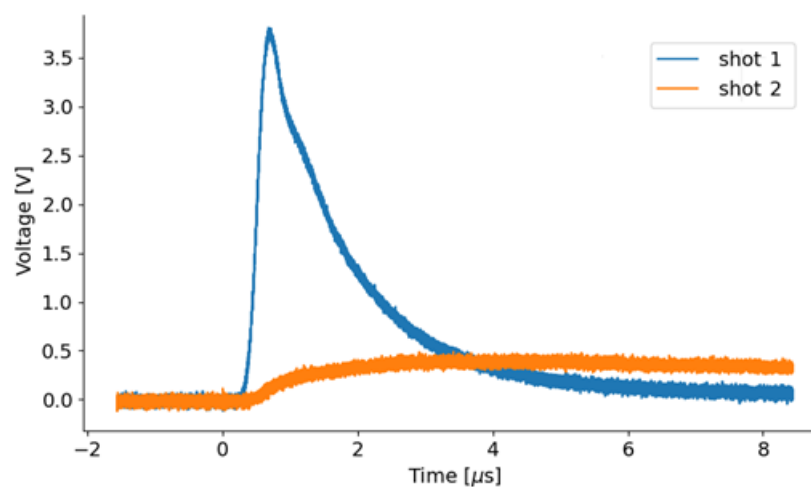


Figure 3. TOF data that were obtained from PERLA 1 kHz laser at intensities of 2.2×10^{16} W/cm² with 2 mm thickness Cu target. Shots 1 and 2 gathered data using the same laser intensity and target parameter specifications under different laser focal sizes due to consecutive laser-target collisions. The X-axis has been adjusted to allow the photopeak to lie on the zero-line for each shot, respectively.

Time-of-flight diagnostics allow for the study of key energy ranges within these datasets via the accurate measurement of ions arrival times with respect to the ion's generation time (which can reliably be estimated to be the time of laser-target collision, as it is orders of magnitude larger than the time over which the acceleration mechanism takes place) [18]. This sudden photopeak spike marks the arrival of soft X-rays that are produced from the laser-target collision and thus acts as an indicator of the "time of release" for the ions. From this information, the time-of-arrival, and thus the kinetic energy of the particles arriving at any given time can be calculated, assuming the particle species is known.

When discussing the maximum kinetic energy that is present within the shot, it is trivial to say that, due to the mass difference across the possible ions, this value is held by the first arriving particles which solely consist of protons, as their decreased mass will ensure a significantly higher velocity and thus a lesser arrival time. We can, therefore, assume that all particles of relevance for this program are hydrogen ions since they are normally present on the target surface as contaminants.

3. Code Functionality

This section details the functionality and development of a simple algorithm to determine the first arrival time of TNSA-generated ions from the above-discussed TOF spectra. Of the 24 datasets, 15 were used as training data while the remaining 9 were used as a confirmation test set, a separate set of data that was not used in the code development but was instead utilized to confirm the validity and functionality of the finished code operating on a set of data hitherto unseen. The development and operation of the code itself will now be discussed before concluding with the validity test.

For the construction of the algorithm to accurately detect the maximum proton energy of a TOF dataset, a similar code that was written in python was used as a baseline. This early code provided two methods of calculation of the maximum proton energy, the former using a basic calculative measure in which the beginning of the curve was taken as the first signal point to exceed the value of three times the standard deviation of the noise data. This value was chosen based on trial and error testing of the code. The latter of the two methods was derived via processing the time-domain data into an energy distribution (the results of which are shown in Figure 1) via Equation (1) as previously shown. The maximum energy could, therefore, be taken from the resulting plots largest energy value.

This code was expanded upon in order to provide a higher level of accuracy for the maximum energy and improved user experience. Below, these changes are detailed, and in the results section we will compare the accuracy of the original and newly designed methods of maximum energy determination (note that, due to the infinitesimal nature of the maximum proton energy, we are limited by the noise floor of the detector and so our maximum energy is defined by some arbitrary conditions, as will be detailed later). Both the original base code and the improved code were constructed exclusively in Python 3.11.0, with data analysis mainly performed using the libraries numpy, pandas, and scipy.

The first step towards accurate energy determination is pinpoint isolation of the photopeak which, due to its often sudden-spiked nature can in most cases be identified within the signal noise. A system was designed to calculate an estimate quantifiable value of the datasets noise by calculating the average of all modulus values and the standard deviation within the first 2% of the data points within the set. This number was manually chosen based on the observation that the photopeak did not lie within this range in any observed data. The modulus values must be used for the averaging process as the noise fluctuates equally about zero, meaning the standard average provides no measurement of the noise magnitude, and the modulus can instead be used to define an average value above zero, about which the signal consistently lies. The photopeak time-of-arrival is then taken as the first voltage signal point to exceed this average modulus noise value plus twice the standard deviation. This formula was again chosen through a trial and error process using the full number of gathered datasets for its development and was found to consistently pinpoint the photopeak to within an acceptably small margin of uncertainty

for all of the datasets provided. This process also defines the photopeak as the rising edge point as opposed to the highest value, however, due to the inherent thinness of the photopeak relative to the datasets full-time scope, this approximation maintains validity (in a dataset of 50,000 points spanning 10 μ s, the photopeak spans five datapoints, or 0.1 ns). This method pinpointed the photopeak exactly in 18 out of the 18 sets in which there was a visible photopeak, however, in the case of the remaining six datasets no photopeak was discernable from the noise due to experimental limitation. For this reason, as well as the thought that there may be datasets in which the photopeak is wrongly pinpointed, the code was thus built in with a manual override, giving the user the option to select a photopeak time by hand when necessary due to the dataset limitations. This can prove useful in situations such as the above, in which the photopeak cannot be seen on the individual set, but its location can be inferred from other sets taken under the same conditions.

To find the beginning of the data curve and thus the maximum proton energy, the gradient was calculated for every point using least squares regression in the range of r points to the left and right of that datapoint. This represents a series of points by the calculated best fit line derived from [19]:

$$m = \frac{NS_{xy} - S_x S_y}{NS_{xx} - S_x^2} \quad \begin{aligned} S_x &\equiv \sum_i x_i \\ S_y &\equiv \sum_i y_i \end{aligned} \quad (2)$$

$$c = \frac{S_{xx} S_y - S_x S_{xy}}{NS_{xx} - S_x^2} \quad \begin{aligned} S_{xy} &\equiv \sum_i x_i y_i \\ S_{xx} &\equiv \sum_i x_i^2 \end{aligned} \quad (3)$$

where x and y are the time and signal values, respectively, m is the gradient of the best fit line, c is the point of Y-axis intersection, all forms of S are self-defined above, and N is the total datapoint count $2r + 1$. The value r , named the range value, was initially arbitrarily assigned, however it was later refined using basic linear regression methods to determine a simple formula for the calculation of an appropriate range value for a new dataset. This process will be covered later in this section.

The process to calculate the local gradient about a point (using Equation (2)) was repeated for every point within the defined point range. From this, a graph of signal change against time can be plotted (Figure 4) which, for a sufficiently large range value, will have greatly reduced noise in comparison to the initial TOF graph (Figure 3). From this relatively noiseless graph, the rising edge can be accurately pinpointed algorithmically based on fluctuations of its own gradient, acting as an accurate prediction of the time-of-arrival of the maximum energy protons. A secondary method which calculated a moving average in place of a gradient calculation was also designed, however later testing (see Section 4) showed a consistently lower accuracy and larger deviation from the value that was gathered by eye for this method and was, therefore, cut from this paper for the sake of brevity.

This raises a key point in the development of this code, however. A small range value will result in a gradient chart with a lesser reduced noise, whereas a large range value will result in over-smoothing of the data and a significant shifting of the curve's rising edge, thus losing accuracy. The system's ability to accurately determine an estimation for maximum proton energy is, therefore, dependent on a procedural range value which must differ for every dataset depending on dataset size and S/N ratio.

While the optimal range value (i.e., the range value which results in the predicted maximum proton energy that is closest to the manually chosen reference value) is unique for each dataset and cannot be predicted specifically (again, due to dataset noise), we can use trends in pre-existing data and basic linear regression techniques to notice trends and patterns that will allow an accurate prediction. A separate, secondary code was developed which calculates an estimate for the beginning of the TOF curve for a given dataset for a series of different range values. For each range value, the calculated prediction for the time-of-arrival is found and compared against the reference answer, a value determined manually by eye which is estimated to be the point at which the curve begins. Through

comparison to the reference value, the range value which gives the most accurate estimation of the minimum TOF for this dataset can be found. By repeating this process for the 15 datasets that were provided, which differ only by signal amplitude, a relationship between the amplitude and the range value was established, which provided a backbone for the development of a set of equations allowing the determination of an approximate optimal range value based on a dataset's characteristics. Of course, due to the inherent nature of the task, i.e., finding an infinitesimal rise in a sea of noise, there cannot be a definitive "correct" value chosen by eye, and as a result this comparison value is an educated estimation at best. However, it acts as a maximum achievable level of accuracy for which we aim for. Through the use of this secondary code, the primary code was fitted with a system to determine an appropriate range value based on pre-determined value bands of S/N ratio, dataset size, and ion load amplitude.

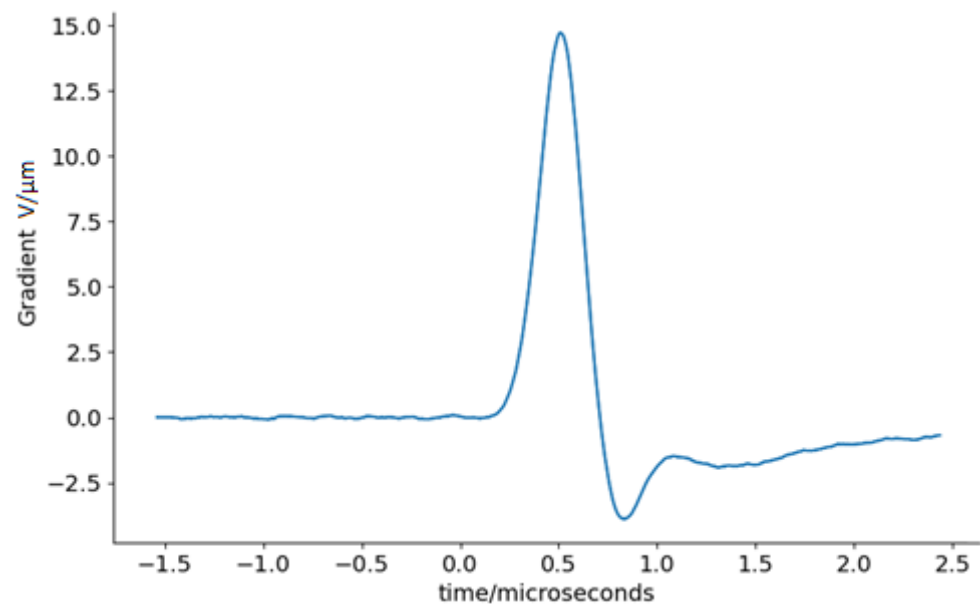


Figure 4. Voltage gradient at each point within the region of interest of Figure 3 shot 1. Dataset size = 40,000 points; range value = 200 points. A drastic decrease in the noise and a clear rising edge can be seen acting as an estimate of the maximum proton energy.

4. Findings and Accuracy

The results of the finished code applied to the nine sets of testing data will now be discussed and compared to the comparative results that were derived from the initially provided two methods, as well as the briefly mentioned average method that was derived as an additional part of this project.

Figure 5 acts as a qualitative comparison of the original simple processing methods of the maximum energy determination to the described gradient method (as well as the aforementioned inefficient average method). These data were the result of processing of the four methods on the first shot shown in Figure 3. As can be seen, the gradient method calculates a deviation from the reference value of 4.2 nanoseconds, compared to the original smallest deviation of 0.092 microseconds (energy distribution calculation) showing a drastically increased accuracy. This pattern was observed across all of the training and testing datasets that were gathered.

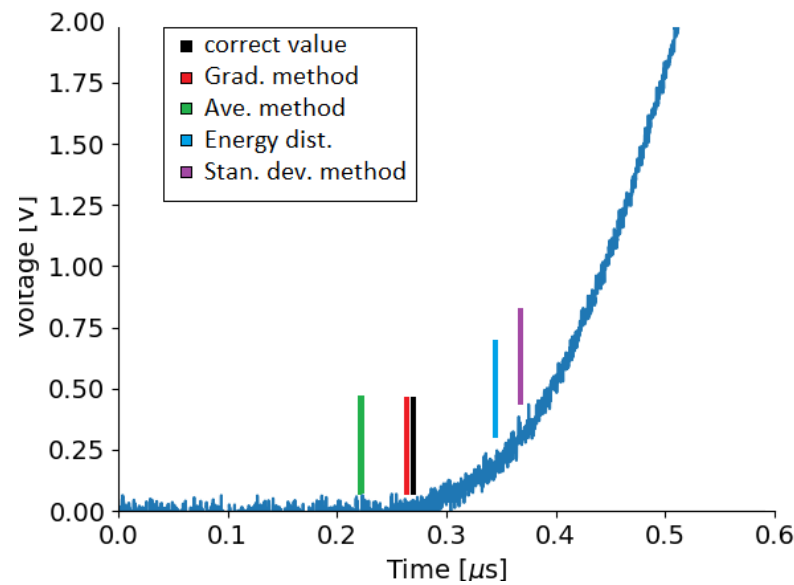


Figure 5. The point determined as the shortest time-of-flight (maximum proton energy) for codes original simplified methods compared to the newly designed algorithms for a single training dataset (Figure 3 shot 1).

Table 1 shows the predicted manually gathered values and calculated values for five of the testing shots. As can be clearly seen, in the time domain a constant high level of accuracy is maintained regardless of S/N ratio, which was significantly higher for the first three shots in comparison to the latter two (a comparison to that seen in Figure 3 can be made). The accuracy was calculated based on the total deviation of the algorithmically selected point from the point that was chosen by eye as a fraction of the overall dataset size within the time domain. Over the 15 training sets, the calculated answer deviated from the manually gathered answer by an average of 0.24% of the dataset, showing a consistently reliable level of accuracy. The deviation was noticeably higher on average for lower S/N ratio shots with a direct proportionality between the two, as can be seen in the data of Table 1 by noting that the shots are arranged in order of decreasing S/N ratio. This is trivial as a more noise-dominant dataset would provide larger complications for the data processing algorithm.

Table 1. Gradient-method calculated predictions of shortest time-of-arrival and corresponding max. proton energies for a number of the training datasets, along with the corresponding equivalent energies. Shots arranged in order of decreasing S/N ratio. The accuracy was calculated from the deviation between estimate and algorithm answers as a percentage of full dataset size.

Shot No.	By-Eye Estimate Time/ μ s	Algorithm Calculated Time/ μ s	By-Eye Estimate Energy/KeV	Algorithm Calculated Energy/KeV	Accuracy %
1	0.206	0.202	3.966	4.125	0.042
2	0.229	0.221	3.207	3.454	0.088
3	0.206	0.191	3.967	4.656	0.163
4	0.414	0.434	0.522	0.897	0.212
5	0.314	0.279	1.709	2.163	0.368

It is worth noting that these results are presented in the time domain as opposed to the energy domain. Despite the energy domains more distinct relevance to the project as a whole, the time domain was chosen to display the project results due to a larger consistency across datasets. As a result of the squared component that is present within

the kinetic energy formula, any error in the time domain will be magnified exponentially upon conversion, providing a less accurate representation of the code's ability to accurately make an estimation of the maximum proton energy. Additionally, slight deviations in the distance value may be magnified within the kinetic energy equation, thus decreasing the accurate representation of the code further.

When run locally, this code is capable of processing the initial 15 datasets in under 0.5 s, a time which can be greatly improved if run on a more specialized device. Nevertheless, the sufficient processing time, as well as the consistently low deviation between the manually selected and calculated values of minimum time-of-flight puts forth the algorithm as a suitable substitute for manual identification and strongly affirms its reliability for the processing of large-scale dataset quantities.

5. Conclusions

In summary, a code was provided to calculate energy distribution spectra and maximum proton energy values from input time-of-flight datasets. The method of maximum proton energy derivation was drastically improved to allow for a more accurate automatic determination of the value via rudimentary machine training techniques, making use of linear regression systems, allowing the code to be fine-tuned using the data. The code was additionally altered to allow functionality for any provided TOF dataset, meaning the proton energy could be predicted to typically within 0.24% margin of error for a universal set of TOF data, regardless of the signal intensity or S/N ratio. Additional feature implementation allowed for the photopeak location to be manually set for situations that may require such a feature, such as cases where no photopeak is visible in an individual dataset but the location of which can be inferred from other data. The code has minimal processing time (>30 datasets/sec, where each set consists of 50,000 points, run on local hardware), and user-friendly systems and annotations have been included for third-party users to easily understand and operate it. Due to the automatic nature of the program, processing of a large number of datasets is possible in quick succession without the need for manual monitoring, suitable for the high-repetition rate that is often achieved with currently available laser systems [20,21] and similarly suitable datasets. The code will be available for free use for the study of TOF data and will prove to be useful in investigations requiring high level accuracy of the laser-accelerated proton spectra characteristics.

The developed code is suitable to systematically analyze a broad range of data that are acquired via laser-plasma experimental campaigns, in particular those aiming at investigating the reliability of laser-driven ion beams for multi-disciplinary applications, including proton insertion in nuclear fusion studies or clinical biomedical research [22].

Author Contributions: The paper's initial idea was proposed by D.M. and E.R.; the experiment was carried out by V.I., Y.L., M.C. and J.H.; data analysis was performed by E.R., V.I. and L.G.; original draft preparation by E.R. review and editing performed by D.M., V.I., L.G., Y.L., M.C., J.H. and M.S. All authors have read and agreed to the published version of the manuscript.

Funding: This work has been supported by the project Advanced research using high-intensity laser-produced photons and particles (CZ.02.1.01/0.0/0.0/16_019/0000789) from European Regional Development Fund (ADONIS) and IMPULSE project by the European Union Framework Program for Research and Innovation Horizon 2020 under grant agreement No 871161. YL acknowledges the support from the European Regional Development Fund and the state budget of the Czech Republic (project BIATRI: No. CZ.02.1.01/0.0/0.0/15_003/0000445). This project has received funding from the European Union's Horizon 2020 research and innovation programme under Grant agreement no. 871124 Laserlab-Europe, Grant agreement no. 739573 HiLASE Centre of Excellence and Operational Programme Research, development, and education under Decision on grant no. 15_006/0000674-01 HiLASE Centre of Excellence.

Institutional Review Board Statement: Not applicable.

Informed Consent Statement: Not applicable.

Data Availability Statement: Data are available from the corresponding authors upon reasonable request.

Acknowledgments: We acknowledge HiLASE Centre in Dolní Břežany, Czech Republic, for provision of laser/experimental station beamtime and would like to thank the instrument group and facility staff for their assistance.

Conflicts of Interest: The authors declare no conflict of interest.

References

1. Bulanov, S.V.; Khoroshkov, V.S.; Daido, H.; Esirkepov, T.; Koga, J.; Nishihara, K.; Pegoraro, F.; Tajima, T.; Yamagiwa, M. Feasibility of using laser ion accelerators in proton therapy. *Plasma Phys. Rep.* **2002**, *28*, 5. [[CrossRef](#)]
2. Yogo, A.; Maeda, T.; Hori, T.; Sakaki, H.; Ogura, K.; Nishiuchi, M.; Sagisaka, A.; Kiriya, H.; Okada, H.; Kanazawa, S.; et al. Measurement of relative biological effectiveness of protons in human cancer cells using a laser-driven quasi mono energetic proton beamline. *Appl. Phys. Lett.* **2011**, *98*, 053701. [[CrossRef](#)]
3. Zylstra, A.B.; Hurricane, O.A.; Callahan, D.A.; Kritcher, A.L.; Ralph, J.E.; Robey, H.F.; Ross, J.S.; Young, C.V.; Baker, K.L.; Casey, D.T.; et al. Burning plasma achieved in inertial fusion. *Nature* **2022**, *601*, 542–548. [[CrossRef](#)] [[PubMed](#)]
4. Barberio, M.; Veltri, S.; Scisciò, M.; Antici, P. Laser-Accelerated Proton Beams as Diagnostics for Cultural Heritage. *Sci. Rep.* **2017**, *7*, 40415. [[CrossRef](#)]
5. Kar, S.; Green, A.; Ahmed, H.; Alejo, A.; Robinson, A.P.L.; Cerchez, M.; Clarke, R.; Doria, D.; Dorkings, S.; Fernandez, J.; et al. Beamed neutron emission driven by laser accelerated light ions. *New J. Phys.* **2016**, *18*. [[CrossRef](#)]
6. Giuffrida, L.; Belloni, F.; Margarone, D.; Petringa, G.; Milluzzo, G.; Scuderi, V.; Velyhan, A.; Rosinski, M.; Picciotto, A.; Kucharik, M.; et al. High-current stream of energetic α particles from laser-driven proton-boron fusion. *Phys. Rev. E* **2020**, *101*, 013204. [[CrossRef](#)]
7. Picciotto, A.; Margarone, D.; Velyhan, A.; Bellutti, P.; Krasa, J.; Szydlowsky, A.; Bertuccio, G.; Shi, Y.; Mangione, A.; Prokūpek, J.E.; et al. Boron-Proton Nuclear-Fusion Enhancement Induced in Boron-Doped Silicon Targets By Low-Contrast Pulsed Laser. *Phys. Rev. X* **2014**, *4*, 031030. [[CrossRef](#)]
8. Borghesi, M.; Fuchs, J.; Bulanov, S.V.; MacKinnon, A.; Patel, P.K.; Roth, M. Fast Ion Generation by High-Intensity Laser Irradiation of Solid Targets and Applications. *Fusion Sci. Technol.* **2006**, *49*, 412–439. [[CrossRef](#)]
9. Passoni, M.; Bertagna, L.; Zani, A. Target normal sheath acceleration: Theory, comparison with experiments and future perspectives. *New J. Phys.* **2010**, *12*. [[CrossRef](#)]
10. Wilks, S.C.; Langdon, A.B.; Cowan, T.E.; Roth, M.; Singh, M.; Hatchett, S.; Key, M.H.; Pennington, D.; MacKinnon, A.; Snavely, R.A. Energetic proton generation in ultra-intense laser–solid interactions. *Phys. Plasmas* **2001**, *8*, 542–549. [[CrossRef](#)]
11. Polanek, R.; Hafz, N.A.; Léc, Z.; Papp, D.; Kamperidis, C.; Brunner, S.; Szabó, E.; Tóké, T.; Hideghéty, K. 1 kHz laser accelerated electron beam feasible for radiotherapy uses: A PIC–Monte Carlo based study. *Nucl. Instrum. Methods Phys. Res. Sect. A Accel. Spectrometers Detect. Assoc. Equip.* **2020**, *987*, 164841. [[CrossRef](#)]
12. Smrž, M.; Novák, O.; Mužík, J.; Turčičová, H.; Chyla, M.; Nagisetty, S.S.; Vylvlečka, M.; Roškot, L.; Miura, T.; Černohorská, J.; et al. Advances in High-Power, Ultrashort Pulse DPSSL Technologies at HiLASE. *Appl. Sci.* **2017**, *7*, 1016. [[CrossRef](#)]
13. Istokskaja, V. A multi-MeV alpha particle source via proton-boron fusion driven by a 10GW Tab-287 let op laser. *Commun. Phys. under review*.
14. Margarone, D.; Krása, J.; Giuffrida, L.; Picciotto, A.; Torrisi, L.; Nowak, T.; Musumeci, P.; Velyhan, A.; Prokūpek, J.; Láška, L.; et al. Full characterization of laser-accelerated ion beams using Faraday cup, silicon carbide, and single-crystal diamond detectors. *J. Appl. Phys.* **2011**, *109*, 103302. [[CrossRef](#)]
15. Doria, D.; Lorusso, A.; Belloni, F.; Nassisi, V. Characterization of a nonequilibrium XeCl laser-plasma by a movable Faraday cup. *Rev. Sci. Instruments* **2004**, *75*, 387–392. [[CrossRef](#)]
16. Roshani, G.; Habibi, M.; Sohrabi, M. An improved design of Faraday cup detector to reduce the escape of secondary electrons in plasma focus device by COMSOL. *Vacuum* **2011**, *86*, 250–253. [[CrossRef](#)]
17. Milluzzo, G.; Scuderi, V.; Alejo, A.; Amico, A.G.; Booth, N.; Borghesi, M.; Cirrone, G.A.P.; Cuttone, G.; Doria, D.; Green, J.; et al. A new energy spectrum reconstruction method for time-of-flight diagnostics of high-energy laser-driven protons. *Rev. Sci. Instrum.* **2019**, *90*, 083303. [[CrossRef](#)]
18. Salvadori, M.; Di Giorgio, G.; Cipriani, M.; Scisciò, M.; Verona, C.; Andreoli, P.L.; Cristofari, G.; De Angelis, R.; Pillon, M.; Andreev, N.E.; et al. Time-Of-Flight methodologies with large-area diamond detectors for ion characterization in laser-driven experiments. *High Power Laser Sci. Eng.* **2022**, *10*, 1–37. [[CrossRef](#)]
19. Iksoon, E. *A Note on Derivation of Least Squares Estimator*; Working Papers; University of Hawaii: Honolulu, HI, USA, 1996; p. 199611.
20. Morrison, J.T.; Feister, S.; Frische, K.D.; Austin, D.R.; Ngirmang, G.K.; Murphy, N.R.; Orban, C.; Chowdhury, E.A.; Roquemore, W.M. MeV proton acceleration at kHz repetition rate from ultra-intense laser liquid interaction. *New J. Phys.* **2018**, *20*, 022001. [[CrossRef](#)]
21. Chagovets, T.; Viswanathan, J.; Tryus, M.; Grepl, F.; Velyhan, A.; Stancek, S.; Giuffrida, L.; Schillaci, F.; Cupal, J.; Koubikova, L.; et al. A Cryogenic Hydrogen Ribbon for Laser Driven Proton Acceleration at Hz-Level Repetition Rate. *Front. Phys.* **2022**, *9*, 754423. [[CrossRef](#)]
22. Margarone, D.; Cirrone, G.P.; Cuttone, G.; Amico, A.; Andò, L.; Borghesi, M.; Bulanov, S.S.; Bulanov, S.V.; Chatain, D.; Fajstavr, A.; et al. ELIMAIA: A Laser-Driven Ion Accelerator for Multidisciplinary Applications. *Quantum Beam Sci.* **2018**, *10*, 8. [[CrossRef](#)]